The Astrophysical Journal Supplement Series, 253:12 (13pp), 2021 March https://doi.org/10.3847/1538-4365/abd4d2

Numerical Research on the Effect of the Initial Parameters of a CME Flux-rope Model on Simulation Results

Fang Shen[1,2,3,4], Yousheng Liu[1,2], and Yi Yang[1,2]
[1] SIGMA Weather Group, State Key Laboratory of Space Weather, National Space Science Center, Chinese Academy of Sciences, Beijing, 100190, People's Republic of China; fshen@spaceweather.ac.cn
[2] College of Earth Sciences, University of Chinese Academy of Sciences, Beijing, 100049, People's Republic of China
[3] Institute of Space Science and Applied Technology, Shenzhen, 518055, People's Republic of China
Received 2020 October 24; revised 2020 December 16; accepted 2020 December 16; published 2021 February 24

Abstract

Coronal mass ejections (CMEs) are the major drivers of space weather, and an accurate modeling of their initialization and propagation up to 1 au and beyond is an important issue for space weather research and forecasts. In this research, we use the newly developed three-dimensional (3D) flux-rope CME initialization model and 3D IN (interplanetary)-TVD MHD model to study the effect of different CME initial parameters on simulation outputs. The initial CME flux model is established based on the graduated cylindrical shell model. In order to test the influence of the CME initial parameters on the simulation results, we try to run several simulations with different CME initial parameters, then investigate the outputs in interplanetary space. Here, we focus only on cases in which observers are located in the same initial direction of propagation of the CME. Our analysis shows that the parameters specifying the CME initialization in the model, including the initial density, the thickness of CME flux tube, initial mass, and initial magnetic field, have different effects on the simulation results for observers near the Earth and Mars, and on the process of propagation of the CME in interplanetary space. This confirms the important role played by details of the initial implementation of geometric and physical parameters on space weather research and forecasts.

Unified Astronomy Thesaurus concepts: Solar coronal mass ejections (310); Solar wind (1534); Corotating streams (314); Magnetohydrodynamical simulations (1966); Space weather (2037)

1. Introduction

A coronal mass ejection (CME) is a phenomenon caused by severe solar activity, which ejects a huge amount of plasma and magnetic flux from the corona into interplanetary space. The CME will destroy the steady flow of interplanetary solar wind, and is considered to be the main source of disastrous space weather such as a geomagnetic storm when it hits the Earth (Gosling et al. 1990). It has been generally believed that a halo CME, which erupts toward the Earth from solar source regions, is the most likely to reach the Earth and to lead to disastrous space weather (e.g., Howard et al. 1982; Gonzalez et al. 1994, 2011; Zhang et al. 2007). When the CME erupts from the solar source regions, there are many initial parameters such as density, velocity, temperature, magnetic field, geometry, etc. All of these parameters will affect the propagation of the CME and its final impact on the Earth and interplanetary space.

A magnetohydrodynamic (MHD) model is one of the effective methods widely used to study and forecast the possible effect of a CME on the Earth. To model the CME propagation, cone models (e.g., Odstrcil & Pizzo 1999; Zhao et al. 2002; Xue et al. 2005), magnetized plasma blob models (Chané et al. 2005), and "spheromak" or "Gibson–Low" flux-rope models (Gibson & Low 1998) are used in the CME initialization. The cone model is one of the popular CME initiation models because of its simplicity and relatively good match with observations of CME arrival times. In most implementations of the cone model, the CME does not possess an internal magnetic field, but the input size, speed, and location are determined from coronal observations, typically from coronagraphs. In addition, due to its geometry and lack of internal magnetic field, the initiation does not include parameters related to CME orientation. Pomoell & Poedts (2018) integrated the cone model into EUHRORIA model to simulate the CME events in the inner heliosphere during 2015 July 17–29. Also by combining the cone model and the EUHRORIA model, Scolini et al. (2018) tested the effect of different CME shapes on the simulation results, and found that all the parameters specifying the CME shape in the model significantly affected the simulation results at 1 au as well as the predicted CME geoeffectiveness.

The magnetized plasma blob model was proposed by Chané et al. (2005, 2006), and described the CME as a high-density, high-pressure, high-speed plasma blob. The most significant difference from the cone model is that it gives the model an initial magnetic field. Moreover, the best fit parameters of the CME initial state can be determined to get a relatively close comparison with ACE data at the L1 point (Chané et al. 2008). By using the 3D corona interplanetary total variation diminishing (COIN-TVD) MHD model with the magnetized plasma blob as the CME initialization model, Shen et al. (2011, 2014b) simulated the time-dependent propagation of single CME events and the interaction of two CMEs events, such as those on 2000 April 4 and 2012 July 12, and the CME–CME interaction event on 2001 March 28. Their simulation could properly reproduce the real 3D nature of the CMEs in

[4] Corresponding author: SIGMA Weather Group, State Key Laboratory of Space Weather, National Space Science Center, Chinese Academy of Sciences, Beijing, 100190, People's Republic of China.

their morphology and their evolution from the Sun to the Earth. Hosteaux et al. (2019) have investigated the propagation of both normal and inverse CMEs with different initial velocities by using a 2.5D MHD model with the magnetized plasma blob CME model, and compared their results of solar wind parameters at 1 au. Their results suggested that the difference of the polarity had little effect on the strength of the shock and the magnitude of the z-component of the magnetic field, but it had an obvious influence on the density peak of the magnetic cloud.

In addition, a CME model called the "spheromak" or "Gibson–Low flux rope model," which was proposed by Gibson & Low (1998), has also been widely applied by several research groups. This model is characterized by its special magnetic field structure, which is described as a spirally twisted toroidal flux rope confined within a sphere. Manchester et al. (2004a, 2004b) have built a 3D numerical ideal MHD model and simulated a CME that is based on the Gibson–Low flux rope model in a steady-state heliospheric environment. They described the morphology and magnetic field structure of the CME in detail near the Sun, and carried out a CME event simulation, which showed the physical parameters of the CME during its propagation. Zhou & Feng (2016) have analyzed and studied the interaction between the CME and the heliospheric current sheet (HCS) by using the 3D SIP-CESE MHD model with the spherical plasmoid flux-rope model. Their research suggests that CMEs tend to deflect toward the HCS in the latitudinal direction near the Sun and then propagate almost parallel to it in interplanetary space.

In our previous work (Liu et al. 2019, cited as Paper I hereafter), a new CME initialization model was established based on the GCS model. The GCS model was an empirical model proposed by Thernisien et al. (2006), which has been widely used in coronagraph observations to study the morphology, position, and kinematics of CMEs (e.g., Liu et al. 2010; Lynch et al. 2010; Patsourakos et al. 2010; Poomvises et al. 2010). This model contained a 3D flux-rope morphological structure and a self-similar expansion form. Because of its characteristic shape, which is that of a curved tubular shell with two thin ends and a thick middle, it is also called the hollow croissant model.

In this work, we use the CME initialization model described in Paper I to test the effect of different CME initial parameters on simulation results at different locations and the geoeffectiveness of the CME. The aim of this work is to study, for our CME initial model based on the GCS model, how the initial density, magnetic field, and thickness of the flux rope influence the CME arrival time and the solar wind parameters at different heliospheric locations, e.g., at the Earth and at Mars. Different implementations result in different CME initial parameters in interplanetary space, each of them leading to different simulation results having potentially significant implications for space weather studies and predictions. Previous works have discussed the effect of different CME parameters, such as the density, velocity, shape, initial magnetic polarity, angular width, as well as the background solar wind and the deflection it causes, on the evolution of a CME, its arrival time at the Earth, and predictions of its geoeffectiveness (e.g., Chané et al. 2005; Shen et al. 2014a; Scolini et al. 2018 and the references therein). Until now, as far as we know, no publications have discussed the effect of the CME initial parameters including its initial density, magnetic field, the thickness of the flux rope, and their combination on the CME arrival time and the solar wind parameters at different interplanetary locations.

In the present paper, by using the improved 3D IN-TVD MHD model (Shen et al. 2018), a stable solar wind background from $21.5R_s$ to $453R_s$ is established first, and then a 3D CME model is built based on the GCS model, which is presented in Section 2. Several groups of CMEs with different initial parameters, including initial density, magnetic field, and geometry, were launched at the same location for comparison, and the result of our simulation is given in Section 3. Section 4 mainly contains the comparison among the different cases at different locations. In Section 5 we summarize the paper and give our discussion.

2. Numerical Simulation Method

2.1. Background Solar Wind Construction with the Improved IN-TVD Model

The improved 3D IN-TVD MHD model (Shen et al. 2018) is used here to construct the background solar wind from $21.5R_s$ to near $453R_s$. In the numerical scheme of the 3D IN-TVD model, all of the physical quantities are computed from the conservation TVD Lax–Friedrich scheme in a Sun-centered spherical coordinate system. For brevity, we do not write the detailed MHD equations here: all of the details can be found in Paper I.

The computational domain covers $21.5R_s \leqslant r \leqslant 453R_s$, $-90^\circ \leqslant \theta \leqslant 90^\circ$ and $0^\circ \leqslant \phi \leqslant 360^\circ$, where the grid mesh is built in the form of $308(r) \times 180(\theta) \times 360(\phi)$. The mesh is uniform in the longitudinal and latitudinal directions with $\Delta\theta = 1^\circ$ and $\Delta\phi = 1^\circ$; in the radial direction, the grid size gradually varies from about $0.37R_s$ at the inner boundary of $21.5R_s$ to $3.61R_s$ at the outer boundary near $453R_s$. To avoid a singularity in the spherical coordinate system, here we use a six-component mesh grid system on the spherical shell (e.g., Feng et al. 2010; Shen et al. 2018; Liu et al. 2019). This grid system consists of six identical component meshes to envelop a spherical surface with partial overlap on their boundaries, and each component grid is a low-latitude spherical mesh.

The Carrington rotation (CR) 2093 is selected to establish the background solar wind. For the interplanetary MHD simulation, the treatment of the inner boundary is very important (Shen et al. 2018). Similarly to Paper I, here we also use the potential field source surface (PFSS) model to extrapolate the coronal magnetic field from the photospheric magnetic field provided by the Global Oscillation Network Group (GONG) project. Actually we do not calculate the coronal region in the simulation of background solar wind because the inner boundary of our model is set at 0.1 au from the solar center. Here our purpose for calculating the coronal magnetic field is to obtain the parameters f_s and θ_b on the source surface, which are necessary configuration parameters of our model. f_s is the expansion factor, which is defined as

$$f_s = \frac{B_s}{B_{ss}}\left(\frac{R_s}{R_{ss}}\right)^2 \quad (1)$$

where B_s and B_{ss} are the magnetic field strengths on the photosphere and on the source surface, respectively; R_s and R_{ss} are the radii of the Sun and of the source surface, respectively. θ_b is the minimum angular distance from the footpoint of a

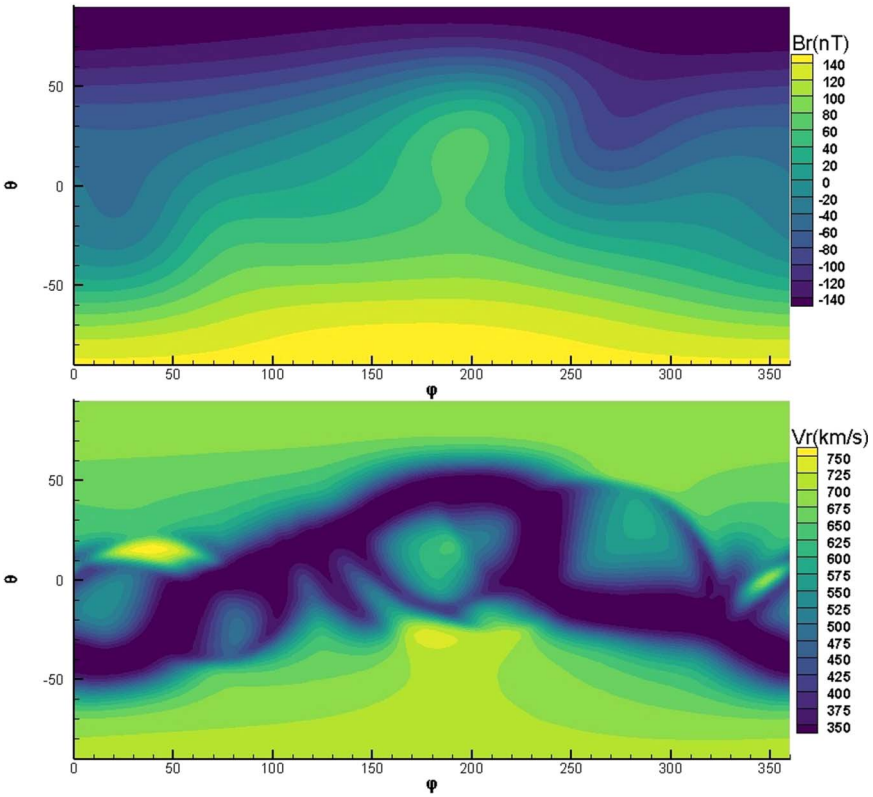

Figure 1. The radial magnetic field distribution according to the PFSS model (top) and the radial velocity distribution based on the WSA model (bottom) on the inner boundary.

magnetic field line at the Sun's surface to the nearest coronal hole boundary.

Then we can initialize the distribution of the solar wind velocity at the inner boundary ($21.5R_s$) with the distribution of f_s and θ_b on the source surface according to the Wang–Sheeley–Arge (WSA) empirical model. The empirical formula of the WSA model can be written as (Arge et al. 2003)

$$V_r = V_s + \frac{V_f}{(1+f_s)^{a_1}}\left[1 - 0.8\exp\left\{-\left(\frac{\theta_b}{a_2}\right)^{a_3}\right\}\right]^{a_4} \quad (2)$$

where V_s means the slowest solar wind speed and V_f is the fastest speed; a_1 to a_4 are free parameters to adjust the solar wind speed in the model. The velocities in the longitudinal and latitudinal directions (V_ϕ and V_θ) are assumed to be zero. There are eight free parameters—V_s, V_f, a_1 to a_4, f_s, and θ_b—which can be adjusted to set different inner boundary conditions for different periods (Shen et al. 2018). Figure 1 shows the distributions of radial velocity and radial magnetic field strength on the inner boundary during CR 2093 that we have built. The inner boundary is given in a fixed way that depends only on the initial parameters and does not change with time; the outer boundary satisfies the nonreflecting boundary condition.

To avoid the accumulation of the $\nabla \cdot \boldsymbol{B}$ error and to satisfy the physical law of $\nabla \cdot \boldsymbol{B} = 0$ during the calculation, here we use a diffusive approach to control it. The $\nabla \cdot \boldsymbol{B}$ error can be diffused away by iterating as follows at each time step:

$$\boldsymbol{B}^{n+1} = \boldsymbol{B}^n + \mu(\Delta x)^2 \nabla\nabla \cdot \boldsymbol{B}^n \quad (3)$$

where

$$(\Delta x)^2 = \frac{1}{\frac{1}{(\Delta r)^2} + \frac{1}{(r\Delta\theta)^2} + \frac{1}{(r\sin\theta\Delta\phi)^2}}$$

in the spherical coordinate system and n is the number of iterations; the value of μ is set to be 0.3 (e.g., Shen et al. 2014b, 2018).

2.2. CME Input with the Graduated Cylindrical Shell (GCS) Model

After establishing the steady-state background solar wind, we model the CME based on the GCS model, just as we did in Paper I. The GCS model was developed by Thernisien et al. (2006, 2009) and Thernisien (2011) to describe the 3D shape and structure of CMEs. The model consists of two main parts: two legs and a curved front. The two legs are conical and the front is reminiscent of a torus with its cross-sectional radius increasing with height. As shown in Figure 2, the half-angle of the cone is denoted as δ. κ is defined as $\sin\delta$, which is called the aspect ratio of the model (Thernisien et al. 2006, 2009; Thernisien 2011). Then, the radius a can be given by $a(r) = \kappa r$, where r is the distance from a point on the shell to the center of the Sun. The angle between the axes of two conical legs is 2α and the height of the cone is h. So the model is described in a self-similar way and we can completely define the geometry of the shell with the three parameters κ, α, and h. A detailed description of the geometric parameters is omitted here for brevity, but can be found in Paper I.

The magnetic field distribution of the CME model is given based on the Lundquist flux-rope model (Lundquist 1951), which is a force-free solution given in cylindrical coordinates

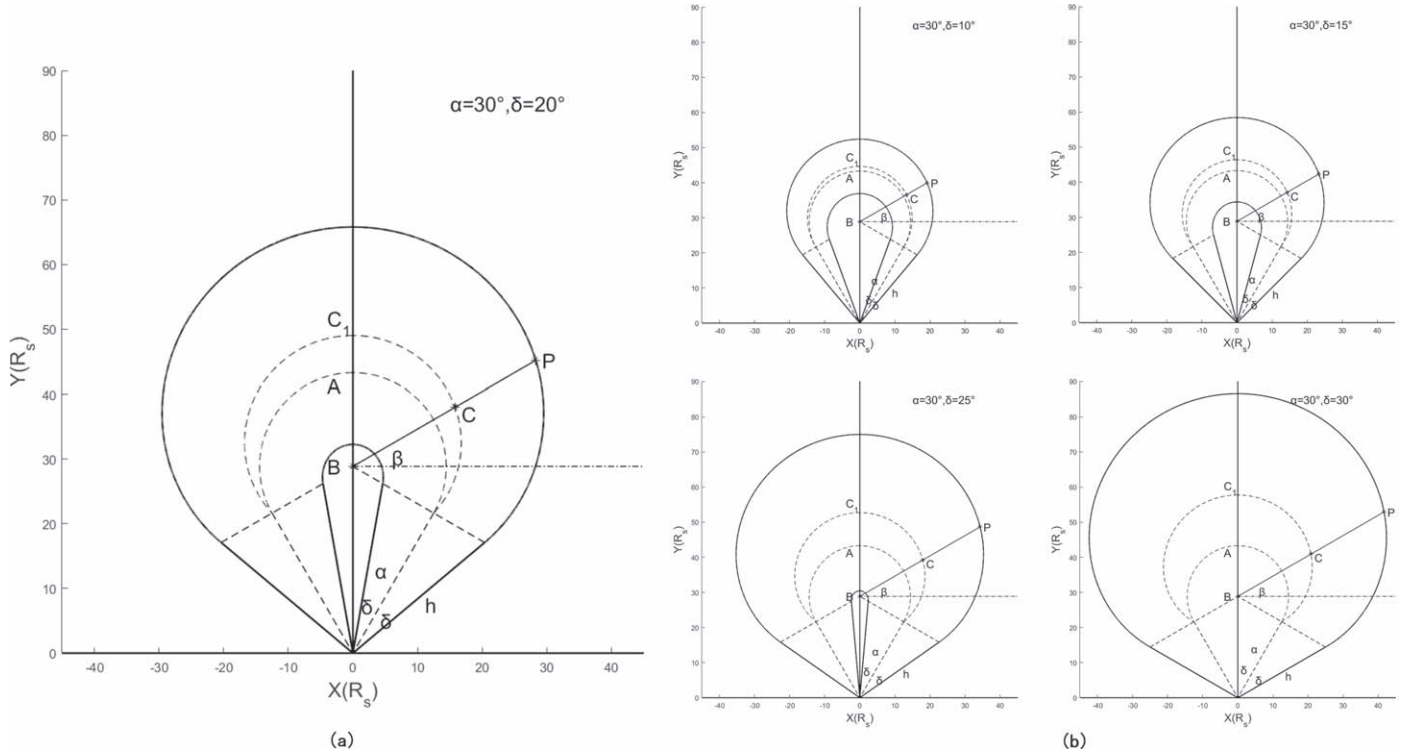

Figure 2. Schematic of the graduated cylindrical shell models with different geometric thicknesses. (a) $\alpha = 30°$ and $\delta = 20°$; (b) $\alpha = 30°$ and $\delta = 10°$, 15°, 25°, and 30°.

$(r; \phi; z)$ as

$$\begin{cases} B_r = 0 \\ B_\phi = \sigma_h B_{\max} J_1(\alpha r) \\ B_z = \sigma_h B_{\max} J_0(\alpha r) \end{cases} \tag{4}$$

where J_1 and J_0 are the first-order and zeroth-order Bessel functions, respectively; $\sigma_h = \pm 1$ is the helicity sign, which stands for the direction of magnetic field; α is the force-free parameter; $B_{\max}$ is the maximum of the magnetic field. We make a standard assumption that the axial component of the magnetic field becomes zero at the edge of the flux rope, i.e., the first zero of J_0 should occur when $r = R$, where R is the radius of the cylindrical shell. We can easily obtain

$$\alpha R \approx 2.405 \tag{5}$$

as proposed by Dasso et al. (2006). The maximum magnetic field $B_{\max}$ of a Lundquist flux rope is written as

$$B_{\max} = \sqrt{\frac{2.405 H_m}{4\pi L R J}} \tag{6}$$

where

$$J = \int_0^R J_1^2(\alpha r)\, dr, \tag{7}$$

H_m is the magnetic helicity of the Lundquist flux rope and L is its length, which can be written as

$$L = 2\omega(H_{\text{front}} - R_{\text{front}}) \tag{8}$$

where ω is the half-angular width of the GCS model, H_{front} and R_{front} are the maximum height and maximum radius of the front.

The density, radial velocity, and temperature profiles of the initial perturbation are defined as follows:

$$\begin{cases} \rho_{\text{cme}} = \rho_{\max}\left(1 - \frac{D^2}{(2R)^2}\right) \\ V_{\text{cme}} = V_{\max}\left(1 - \frac{D^2}{(2R)^2}\right) \\ T_{\text{cme}} = T_{\max}\left(1 - \frac{D^2}{(2R)^2}\right). \end{cases} \tag{9}$$

The total density, radial velocity, and temperature of the CME area can be written as

$$\begin{cases} \rho_{\text{total}} = \rho_{\text{cme}} + \rho_0 \frac{D^2}{(2R)^2} \\ V_{\text{total}} = V_{\text{cme}} + V_0 \frac{D^2}{(2R)^2} \\ T_{\text{total}} = T_{\text{cme}} + T_0 \frac{D^2}{(2R)^2}. \end{cases} \tag{10}$$

In the front part of the flux rope, R is the radius of the cross section at the different position, and D is the distance to the central point B; in the conical legs, R still represents the radius of the cross section, but D is defined as the distance to the inner side of the cone in the cross-sectional plane. $\rho_{\max}$, $V_{\max}$, and $T_{\max}$ are the maximum density, radial velocity, and temperature of the CME. ρ_0, V_0, and T_0 are the density, radial velocity, and temperature of the background solar wind, respectively.

3. Selection of Test Cases and Simulation Results

In this work, we choose 18 test cases with different CME initial parameters and try to investigate the outputs at different positions in interplanetary space. The CME initial parameters of these cases are presented in Table 1. In the 18 cases, we keep

Table 1
CME Initial Parameters of the 18 Cases

Common Par.	Direction					V_{max}				T_{max}				h		α		
	N0W0					1200 km s^{-1}				1.5×10^6 K				$25R_s$		30°		
Other Par.	Standard case	I: Varied initial density				II: Varied geometric thickness				III: Varied initial density and geometric thickness with same total mass				IV: Varied initial magnetic field				
	Case 1	Case 2	Case 3	Case 4	Case 5	Case 6	Case 7	Case 8	Case 9	Case 10	Case 11	Case 12	Case 13	Case 14	Case 15	Case 16	Case 17	Case 18	
$\rho_{max}(10^{-18}$ kg $m^{-3})$	1.0	0.2	0.5	2.0	5.0	1.0	1.0	1.0	1.0	5.42	2.12	0.509	0.267	1.0	1.0	1.0	1.0	1.0
δ (deg)	20	20	20	20	20	10	15	25	30	10	15	25	30	20	20	20	20	20
H_m $(10^{42}$ $Mx^2)$	1.0	1.0	1.0	1.0	1.0	1.0	1.0	1.0	1.0	1.0	1.0	1.0	1.0	1.0	5.0	0.2	0.2	1.0	5.0
σ_h	1.0	1.0	1.0	1.0	1.0	1.0	1.0	1.0	1.0	1.0	1.0	1.0	1.0	1.0	1.0	1.0	−1.0	−1.0	−1.0

Note. The top two rows list the common initial parameters and the other rows list the different initial parameters. The common initial parameters (left to right) are the propagation direction, the maximum velocity and temperature of the initial CME, the height of the GCS cone, and the half-angle between the axes of two conical legs, respectively. The different initial parameters, from top to bottom, are the maximum density of the initial CME, the half-angle of the GCS cone, the magnetic helicity of the initial flux rope, and the helicity sign.

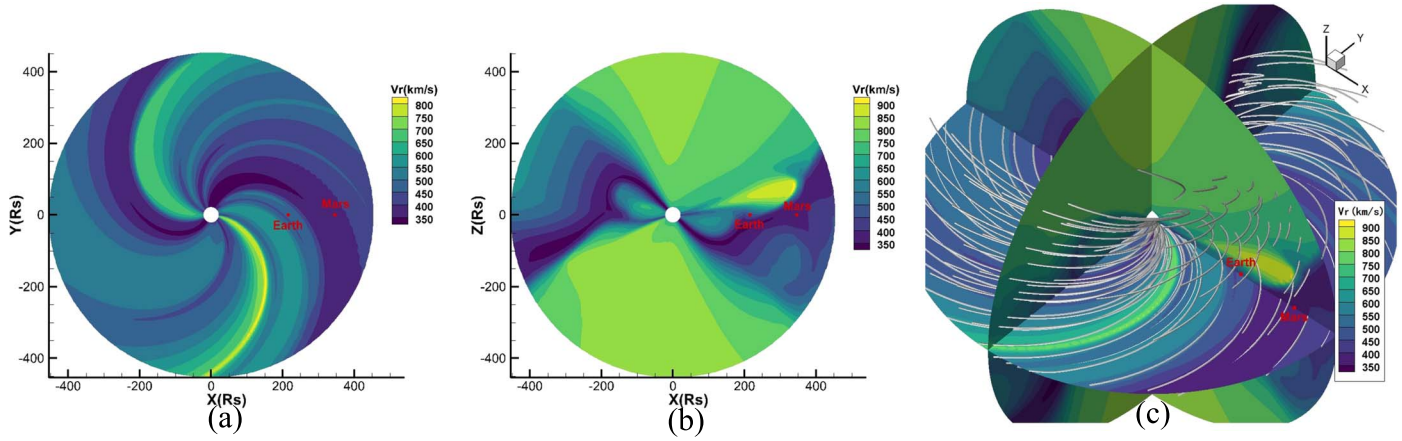

Figure 3. The steady-state distribution of radial velocity (panels (a)–(c)) and magnetic field lines (panel (c)). Panels (a) and (b) show the ecliptic plane and the meridian plane of $\phi = 0°$, and (c) shows a 3D image. The locations of the Earth and Mars are marked with red dots in the three panels.

a few conditions unchanged, including the background solar wind, the initial input position and direction, the maximum velocity and temperature of the initial CME, and the height and radius of the GCS cone. And we test a broad range of the maximum density of the initial CME, the half-angle of the GCS cone, the combination of density and half-angle, and the magnetic helicity of the initial flux rope with helicity sign.

3.1. Propagation of the CME in Interplanetary Space

When the boundary and initial conditions are given, it takes about 400 hr to reach the MHD equilibrium state. The distributions of density, velocity, and the magnetic field lines of the background solar wind on the ecliptic plane are shown in Figure 3. In the steady state, the flow field and magnetic field of the background become spiral. Distinct compression regions with relatively higher density and lower velocity can also be found in Figure 3.

Similar to Paper I, in order to show the compression structure in the longitudinal direction more clearly, the density N is transformed to N^* as follows:

$$N^* = N \times \left(\frac{r}{215R_s}\right)^2 \tag{11}$$

where r is the radial distance. In this way, the attenuation of density due to the increase in radial distance will be reduced and the difference in longitudinal direction will be shown more clearly.

After the ambient solar wind is established, we launch the initial CME based on the GCS model toward the Earth, which is at $\phi = 0°$. The initial parameters of the CME are shown as Case 1 in Table 1. Figure 4 shows the distribution of density, radial velocity, and magnetic field lines at $t = 20$, 60, and 100 hr after launch of the CME on the background. We can see that the CME propagates along an Archimedean spiral in the ecliptic plane due to the influence of centrifugal force in the rotating coordinate system. The main body of the CME expands gradually and forms a high-density and high-velocity region at its front side along its propagation direction where the magnetic field also begins to accumulate. In Figures 3 and 4, the locations of the Earth and Mars are marked with red dots. In CR 2093, Mars is at a heliocentric distance of $346R_s$ and at almost the same latitude and longitude as the Earth.

3.2. Varied Initial Density

To study the influence of the CME initial parameters on its propagation and the plasma parameters at different locations in interplanetary space, we start with the initial density of the CME. First, we take the parameters of the CME in Section 3.1 as the standard case, which is marked as Case 1 in Table 1. For Case 2 to Case 5, the values of initial maximum number density are varied from 20% to 500% of the standard case, with other parameters remaining unchanged, as shown in Table 1. The results of Cases 1–5 are shown in Figure 5.

From Figure 5, it can be found that increasing the initial density of the CME can shorten the CME arrival time and obviously increase the peak values of density, radial velocity, and total magnetic field strength of the CME, both at the Earth and at Mars, while the south magnetic field is affected only slightly.

3.3. Varied Geometric Thickness

In addition to the physical parameters of the CME, the geometric parameters of the CME model may also affect its propagation (Scolini et al. 2018). Compared with the height h and angle α, which can be obtained easily from observation, the vertex angle δ of the model's conical legs has greater flexibility. From Figure 2, it can be easily found that δ mostly controls the thickness of the CME flux tube.

It is worth noting that although the parameters V and B are calculated based on Equations (4)–(10), changing the initial value of geometric thickness δ will not affect the distribution of V and B obviously. Equations (4)–(10) are designed to describe a distribution pattern in which the maximum of the parameter values is located at the CME center, and the values then gradually decrease to the same level as the background solar wind. Therefore, changing the geometric thickness does not change this kind of distribution, it only enlarges or reduces the CME by the same proportion.

Besides Case 1, Cases 6–9 compare different δ values, which are 20°, 10°, 15°, 25°, and 30°. The results of Case 1 and Cases 6–9 are shown in Figure 6.

From Figure 6, we can see that as the initial δ increases, that is, as the CME becomes thicker, its arrival time becomes obviously shorter, and the peak values of density, radial velocity, and total magnetic field strength of the CME all increase obviously, both at the Earth and at Mars. Combined

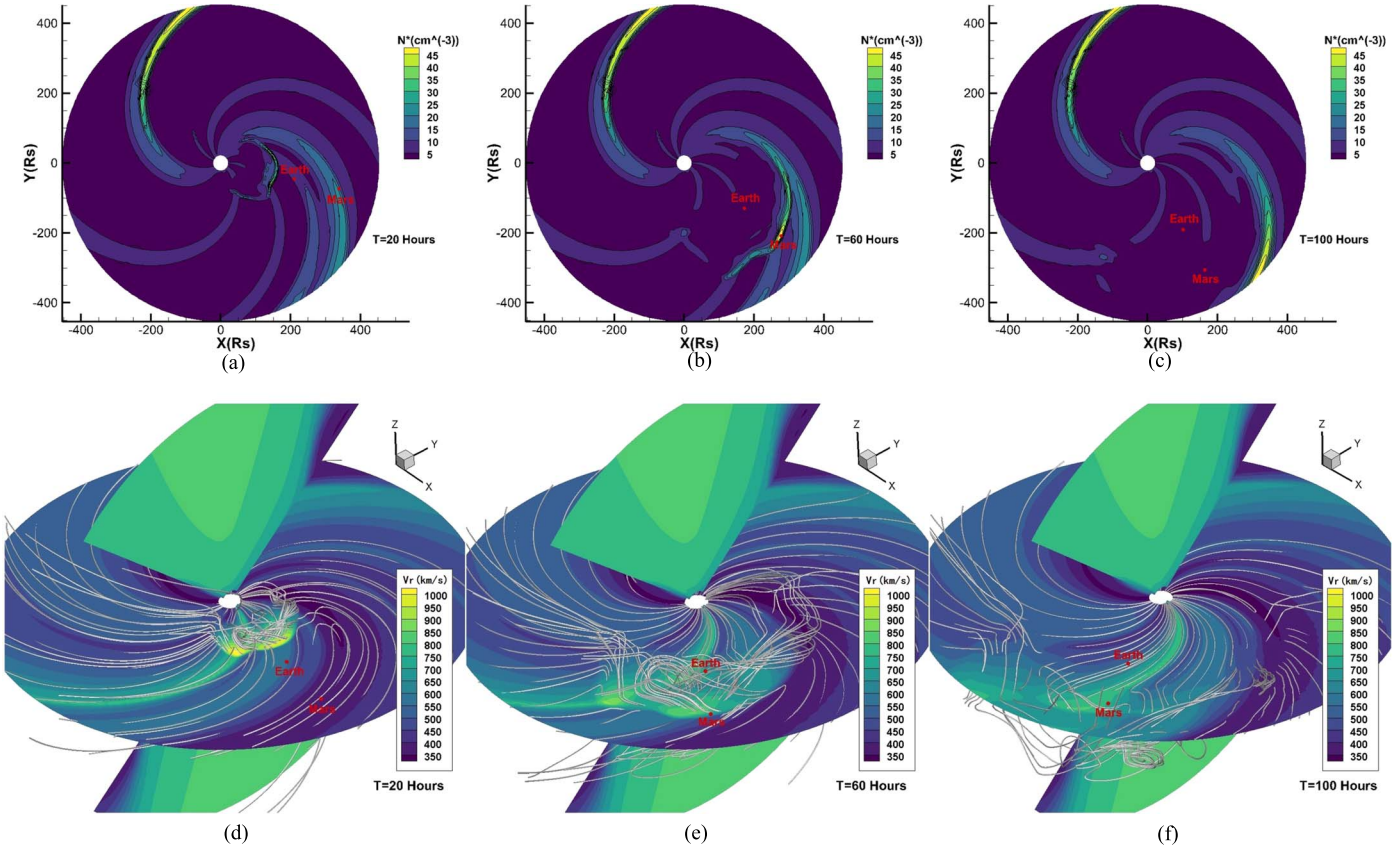

Figure 4. The distribution of density on the ecliptic plane (top panels), radial velocity and magnetic filed lines (bottom panels) at different time. Panels (a) and (d) are at the time of 20 hr; panels (b) and (e) are at the time of 60 hr; panels (c) and (f) are at the time of 100 hr. The locations of the Earth and Mars are marked with red dots in the figure.

with the results in Section 3.2, we find that there are some similarities between the two groups of cases. No matter whether the density or the size increases, it eventually leads to an increase in the initial total mass. From the result of the two groups, it is likely that the initial total mass is the key factor to determine the arrival time, arrival velocity, magnetic field strength, and duration.

3.4. Varied Initial Density and Geometric Thickness with Same Total Mass

To verify the idea in Section 3.3, in the following we will vary the thickness of the CME and the initial density at the same time, with the initial total mass of CME approximately unchanged. In order to calculate the total mass of the CME, we need to calculate its volume based on the GCS model. This GCS model mainly consists of two parts: two conical legs and a curved front. The volume of a conical leg is analytical and easy to calculate. To calculate the volume of the curved front, we integrate the volume along the β direction with point B as the center, as shown in Figure 2. We know that the cross section of the model in the plane ($\vec{BP}$, z) is a circle, and its radius R has the following relationship with β:

$$R^2(\beta) = \left(\frac{\rho + b\kappa^2 \sin\beta}{1-\kappa^2}\right)^2 + \frac{b^2\kappa^2 - \rho^2}{1-\kappa^2}. \tag{12}$$

So the volume of the curved front is

$$V_f = \int_{-\alpha}^{\pi+\alpha} \pi R^2(\beta) \times \mathrm{BC}(\beta)\, d\beta \tag{13}$$

where

$$\mathrm{BC}(\beta) = \frac{\rho + b\kappa^2 \sin\beta}{1-\kappa^2} \tag{14}$$

and the total volume of the initial CME is

$$V_{\mathrm{total}} = V_f + 2\frac{\pi(h\tan\delta)^2 h}{3} - 2\frac{2\pi(1-\cos\delta)\times 21.5^3}{3}. \tag{15}$$

In this way, Cases 10–13 are given with different initial thicknesses and densities, with the same total mass as Case 1, as shown in Table 1. The results of Case 1 and Cases 10–13 are shown in Figure 7.

In Figure 7, when both the initial size and the density of CMEs are different while their total mass remains unchanged in the five cases, we can clearly see that the results of Case 1 and Cases 10–13 are very close in CME arrival time, peak values of density, velocity, total magnetic field, and south magnetic field, both at the Earth and at Mars. These results imply that in the initial factors that affect the simulation results at different locations in interplanetary space, the initial total mass of CMEs is probably much more important than their initial shape and initial density.

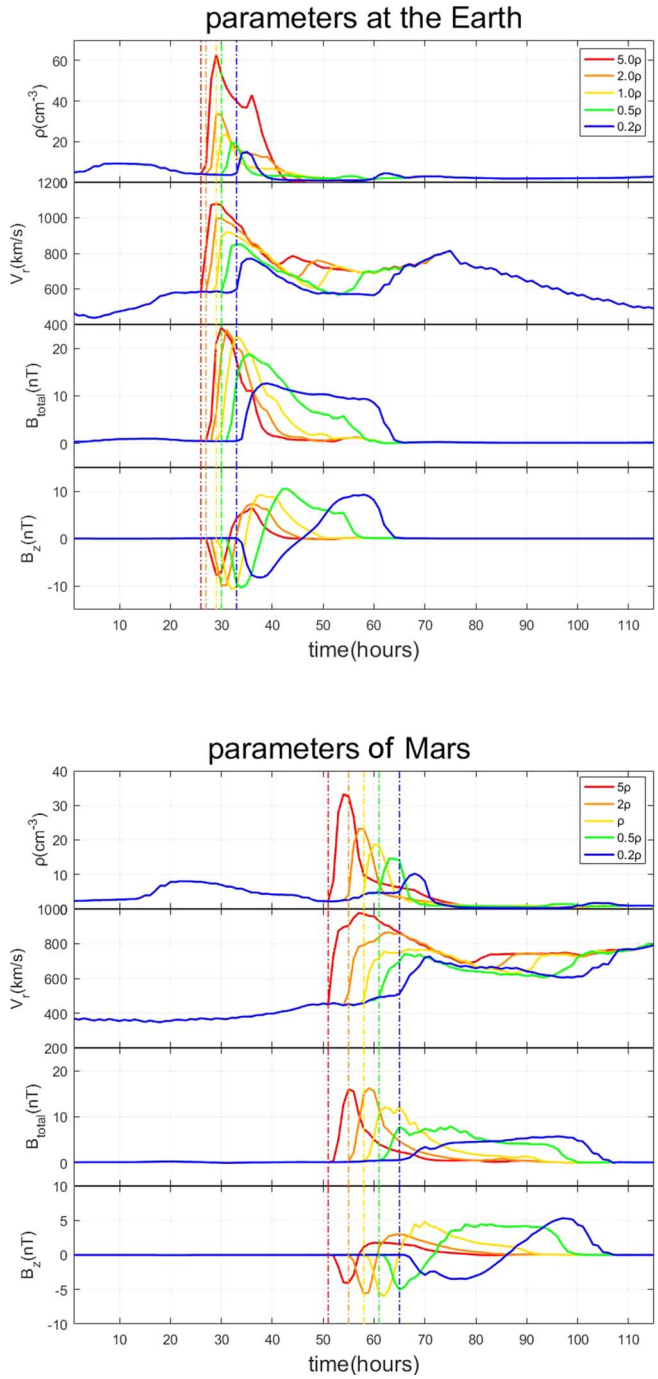

Figure 5. The profiles of plasma parameters–density, radial velocity, total magnetic field strength $B_{\rm total}$, and B_z—at the Earth (top) and Mars (bottom) vs. time after CME launch. Curves with different colors refer to Cases 1–5 listed in Table 1: yellow, blue, green, orange, and red lines indicate Cases 1, 2, 3, 4, and 5, respectively. The shock arrival times of different CMEs are marked by dashed–dotted vertical lines with different corresponding colors.

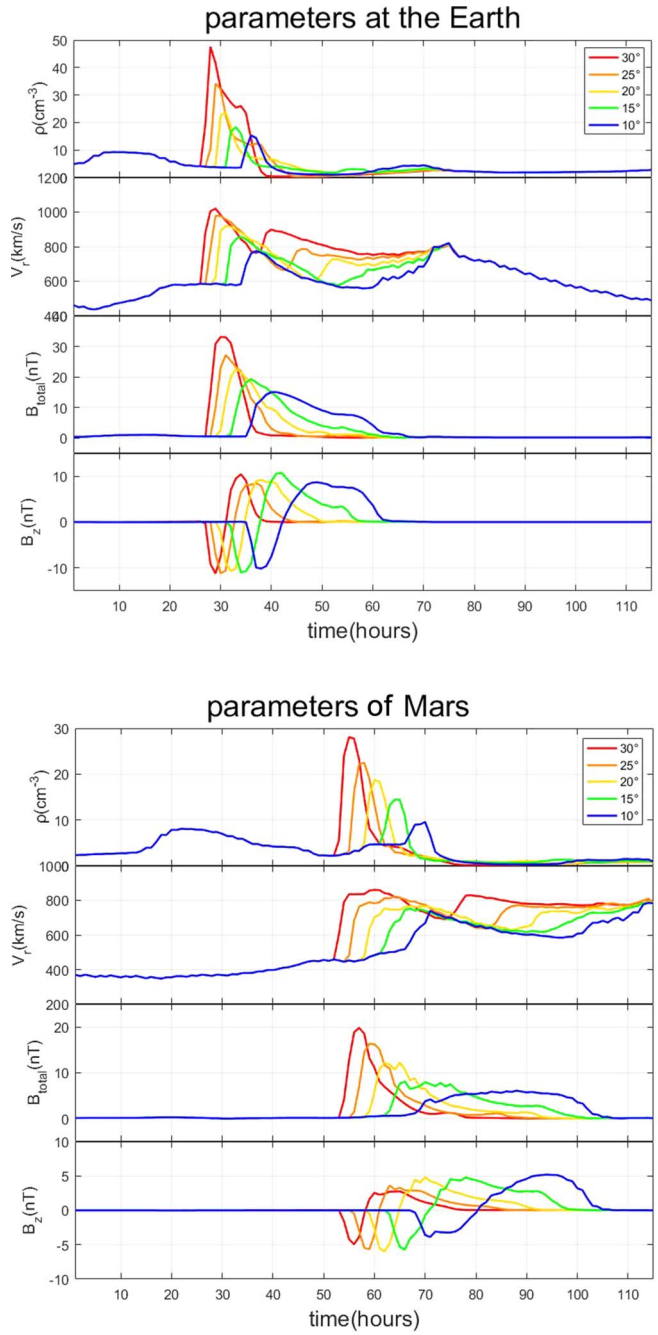

Figure 6. The profiles of plasma parameters—density, radial velocity, total magnetic field strength $B_{\rm total}$, and B_z—at the Earth (top) and Mars (bottom) vs. time after CME launch. The curves with different colors refer to Case 1 and Cases 6–9 listed in Table 1: yellow, blue, green, orange, and red lines indicate Cases 1, 6, 7, 8, and 9, respectively.

3.5. Varied Initial Magnetic Field

Finally, we try to vary the initial maximum magnetic field helicity, including the helicity sign. In Cases 14 and 15, the values of the initial magnetic field helicity, $B_{\rm max}$, are set as 500% and 20% of the standard value in Case 1, respectively. Then the value σ_h in Equation (4) is set to -1 and the magnetic field helicity is set as 20%, 100%, and 500% of the standard value, as shown in Cases 16–18. The results of Case 1 and Cases 14–18 are shown in Figure 8.

From Figure 8, we can see that a change in the initial magnetic field, whether in sign or strength, has little effect on the profiles of the density and velocity curves of the CME. Both the arrival time and the peak values of the density and velocity of CMEs show little difference at the locations of the Earth and Mars when the initial magnetic field strength varies. As the initial magnetic field strength increases, both the peak value of the total magnetic field and the duration of the prominence of $B_{\rm total}$ and B_z also increase obviously at the

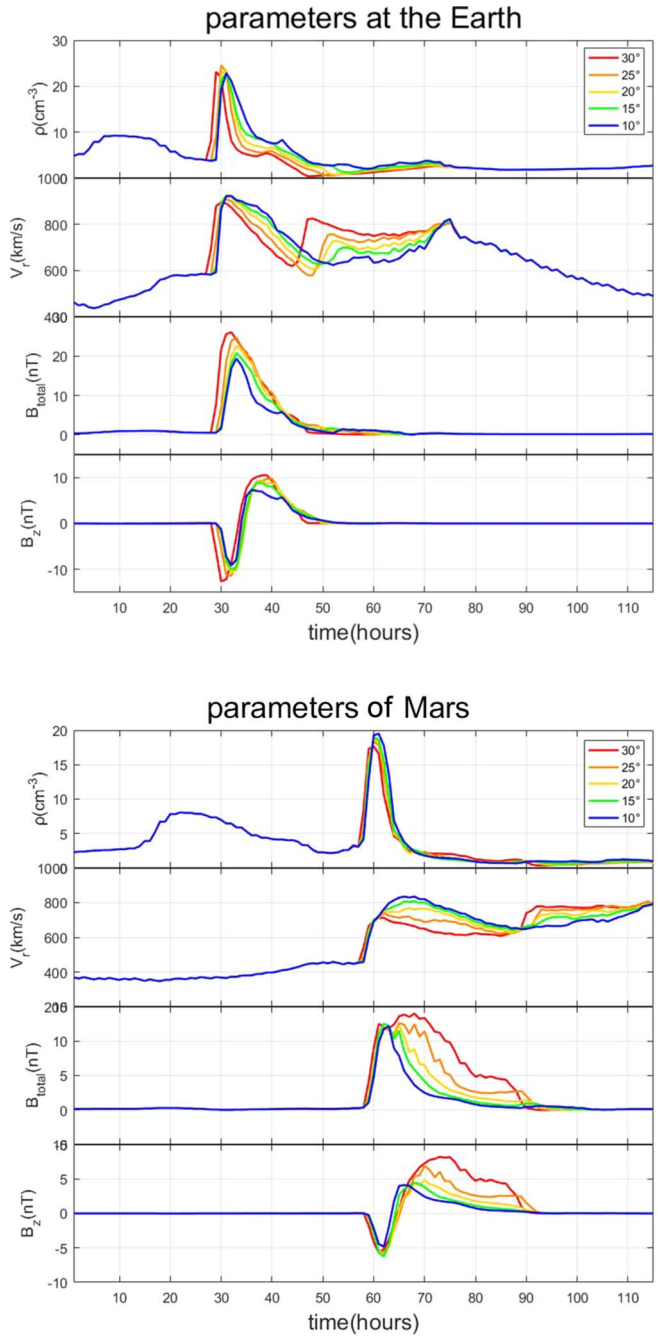

Figure 7. The profiles of plasma parameters—density, radial velocity, total magnetic field strength $B_{\rm total}$, and B_z—at the Earth (top) and Mars (bottom) vs. time after CME launch. The curves with different colors refer to Case 1 and Cases 10–13 listed in Table 1: yellow, blue, green, orange, and red lines indicate Cases 1, 10, 11, 12, and 13, respectively.

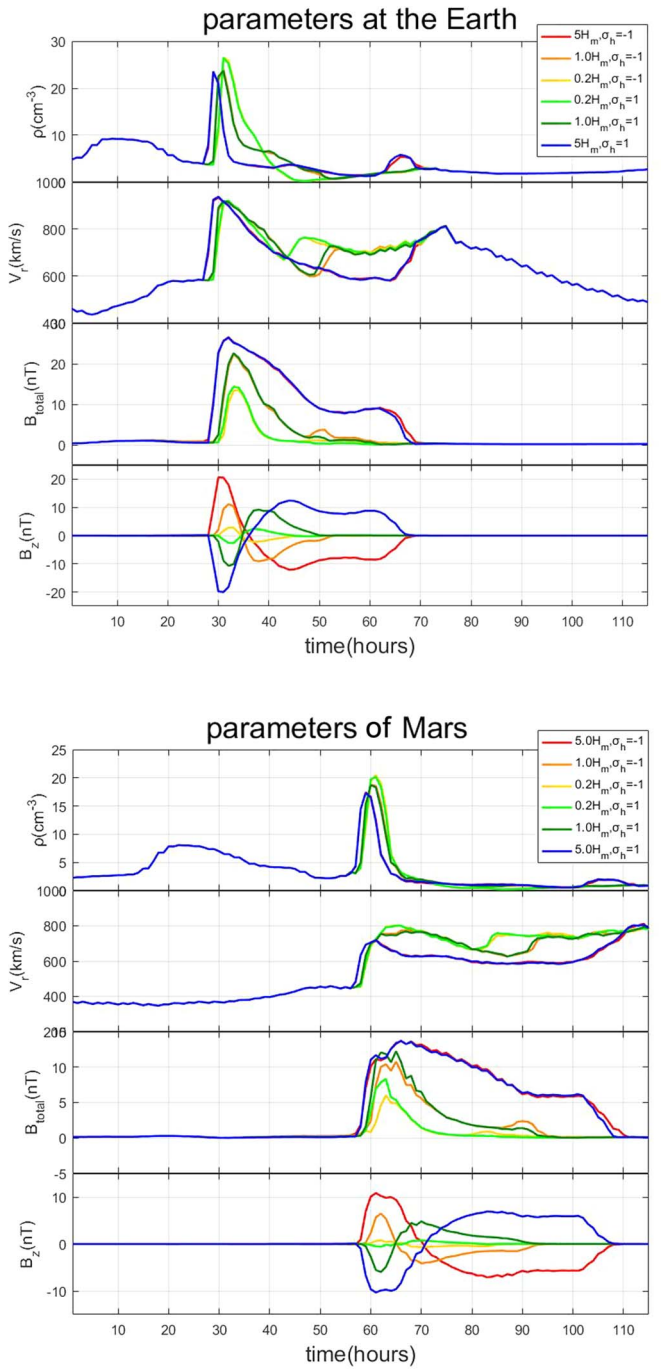

Figure 8. The profiles of plasma parameters—density, radial velocity, total magnetic field strength $B_{\rm total}$, and B_z—at the Earth (top) and Mars (bottom) vs. time after CME launch. The curves with different colors refer to Case 1 and Cases 14–18 listed in Table 1: dark green, blue, light green, yellow, orange, and red lines indicate Cases 1, 14, 15, 16, 17, and 18, respectively.

locations of the Earth and Mars. Besides, as the sign of the magnetic field is reversed, only the direction of B_z is opposite, while other parameters, such as the density, velocity, and $B_{\rm total}$, are almost identical, both at the Earth and Mars.

4. Comparison among the Different Cases at Different Locations

In order to study the in situ properties of the CME in interplanetary space, we make a series of comparisons among different cases, as shown as Table 1, at different locations, which are shown as the Earth and Mars in Figure 3. Table 2 provides the quantitative comparison among the simulation results of the 18 cases, including the shock arrival time (SAT), peak values of radial velocity, number density, total magnetic field, south B_z, duration of south B_z, and the sign of B_z, both at the Earth and at Mars.

4.1. Shock Arrival Time (SAT)

In this study, the shock front is defined by the jump in the density. When the rate of change of density is greater than a

Table 2
Simulation Results of the 18 Cases

Result		Case 1	Case 2	Case 3	Case 4	Case 5	Case 6	Case 7	Case 8	Case 9	Case 10	Case 11	Case 12	Case 13	Case 14	Case 15	Case 16	Case 17	Case 18
SAT (hr)	at Earth	29	33	30	27	26	34	31	27	26	29	29	28	27	27	29	29	29	27
	at Mars	58	65	61	55	51	66	61	55	52	58	58	57	57	57	58	58	58	57
Peak value	at Earth	920	780	840	1000	1080	740	830	990	1020	940	920	920	900	940	920	920	920	940
of V_r (km s^{-1})	at Mars	760	720	740	860	980	740	740	800	880	840	800	740	720	740	780	780	760	740
Peak value	at Earth	24	16	20	34	62	16	18	34	48	23	23	25	24	26	24	24	24	26
of ρ (cm^{-3})	at Mars	19	10	15	23	32	10	15	22	29	20	19	18	18	17	20	20	19	17
Peak value	at Earth	22	12	19	23	24	16	20	26	32	19	21	24	26	26	14	14	22	26
of $B_{\rm total}$ (nT)	at Mars	12	6	8	16	16	6	8	16	20	12	12	12	14	14	8	5	11	14
Peak value	at Earth	−10	−8	−10	−10	−7	−10	−11	−11	−11	−9	−10	−11	−12	−20	−2	−2	−9	−12
of south B_z (nT)	at Mars	−6	−4	−5	−6	−4	−4	−6	−6	−5	−5	−6	−6	−6	−10	−1	−1	−4	−7
Duration	at Earth	6	11	8	5	4	7	6	5	4	5	6	6	6	9	5	9	18	31
of south B_z (hr)	at Mars	7	19	10	6	5	12	8	6	5	5	6	7	7	14	6	18	27	38
Sign of	at Earth	−+	−+	−+	−+	−+	−+	−+	−+	−+	−+	−+	−+	−+	−+	−+	+−	+−	+−
B_z	at Mars	−+	−+	−+	−+	−+	−+	−+	−+	−+	−+	−+	−+	−+	−+	−+	+−	+−	+−

Note. From top to bottom: shock arrival time (SAT), peak values of radial velocity (V_r), number density (ρ), total magnetic field ($B_{\rm total}$), magnetic field in the z-direction (B_z), duration of south B_z, and the sign of B_z, at the Earth and Mars,.

certain constant Q, which can be written as

$$\frac{\rho_i - \rho_{i-1}}{\Delta t} \geqslant Q, \tag{16}$$

we can consider it as the arrival of the shock front. ρ_i is the density at the observer at that moment; ρ_{i-1} is the density here at the previous moment (one hour ago); Q here is set to 8 cm^{-3} h^{-1}.

The SATs of Cases 1–5 are shown by the vertical dashed lines in Figure 4. From the first row of Table 2, by comparing the SATs at the two locations in the same Cases, we can see that the SAT at Mars is almost twice that at the Earth. We take Case 1 as an example: the distance from the CME initial front to the Earth (S1) is about 175 R_s and that from the Earth to Mars (S2) is about 131 R_s, while the SATs of S1 and S2 are almost identical. The average velocity of the CME front propagating in S1 is about 1127 km s^{-1}, and that in S2 is about 844 km s^{-1}. This indicates that as the fast CME propagates in interplanetary space beyond 1 au, it also decelerates obviously.

Furthermore, the quantitative comparison of SATs among the 18 cases in Table 2 also confirms that the initial total mass of the CME is a very important factor in determining the SAT, while a change in initial magnetic field has little effect on the SAT.

4.2. Peak Value of Plasma Parameters of the CME

In addition to the SAT, the CME initial parameters also affect the strength of the impact when it reaches the locations of the Earth and Mars. From the peak value of each plasma parameter, shown in the second to the fifth rows of Table 2, we can clearly see that when the initial density or size increases, the peaks of density and velocity are significantly improved. At the same time, the overall magnetic field will also show a compressed trend, which makes the peak value of B_{total} rise; but there is no obvious change in the peak value of B_z. Besides, when we adjust the initial density and size of the CME to keep its initial total mass unchanged, the peak values of density, velocity, and magnetic field will be approximately unchanged.

Meanwhile, the adjustment of the initial magnetic field can hardly affect the peak value of density and velocity; instead, it has a great influence on the magnetic field. As the magnetic helicity of the initial magnetic field is increased, the peak values of B_{total} and B_z at the Earth and Mars will increase accordingly. Comparing the peak values at the Earth and at Mars, we find that all the peak values at the Earth are larger than those at Mars, including density, velocity, and total and z-component magnetic fields.

Besides, from the Earth to Mars, the peak values of density, velocity, and magnetic field are all decreasing. But in Table 2 we can see that the reduction in magnetic field is significantly greater than those in density and velocity. In most cases, the peak of magnetic field B_{total} and south B_z at Mars are only about half of those at the Earth, while the peaks of density and velocity at Mars are generally maintained at two-thirds or more of their values at the Earth. This indicates that the density and velocity of the CME are less affected by the background solar wind than the magnetic field during the CME's interplanetary propagation, which also reflects that the dynamic factor of the CME is more dominant than its magnetic field in interplanetary space.

4.3. Duration of South $\mathrm{B_z}$

It is known that the initial magnetic field polarity inside a flux rope plays a very important role in the evolution of CMEs; in particular, a different magnetic flux-rope polarity leads to a different magnetic field configuration (Chané et al. 2005). As shown in Tables 1 and 2, for cases 1–15, if the helicity sign of the initial magnetic field σ_h is set as 1, B_z of the CME will be southward first and then change to northward when the CME passes by the Earth and Mars. Otherwise, for cases 16–18, if σ_h is set as -1, B_z of the CME will be northward first and then change to southward.

Combining the view of B_z panels in Figures 5–8 and the quantitative results in the sixth row of Table 2, it can be found that (1) the larger the initial mass of CME is, the shorter the duration of the south B_z, as shown in Cases 1–9; (2) the stronger the initial magnetic field is, the longer the duration of south B_z, as shown in Cases 1 and 14–18; (3) whether σ_h is set as 1 or -1, the duration of B_z in its second stage (after it changes its sign) will be always longer than its duration in its first stage (before it changes its sign); (4) the duration of south B_z at the Earth is significantly smaller than that at Mars.

At the front edge of the CME, the magnetic field is compressed by the structure of high density and velocity, while at the back of the CME, it is not compressed. Therefore, the duration of the second stage of B_z is always longer, e.g., in Cases 16–18. Similarly, when we increase the initial total mass of the CME, including increasing its initial density or size, the magnetic field tends to be more compressed when the CME arrives at the observers. Therefore, the factor of initial total mass also affects the duration of south B_z obviously.

5. Summary and Discussion

In this paper, we have numerically investigated the influence of the CME's initial parameters, including density, geometry, total initial mass, and magnetic field of the CME, on the simulation results at observers near the Earth and Mars. CR 2093 is chosen for our study, because the Earth and Mars are in almost the same direction in this period. A steady-state interplanetary background solar wind is established by a 3D IN-TVD MHD model first. Then we established 18 groups of CMEs based on the GCS model. By adjusting the initial parameters of the CME in different groups, we ran 18 cases of different results for comparison and analysis. The 18 cases comprised one standard case, four cases with varied initial density, four cases with varied geometry, four cases with varied initial density and varied geometry but the same total mass, and five cases with varied initial magnetic field.

We find that the different initial parameters have different effects on the simulation results at observers near the Earth and Mars, and on the process of CME propagation. Changing the initial density or geometric size of the CME will affect its propagation, which includes its arrival time at the Earth and Mars, and its velocity when propagating in interplanetary space. When the initial density and geometric dimensions of the CME are changed simultaneously, they will both affect its propagation. Further simulation shows that when the initial density and geometric dimensions of the CME are both changed, the process of propagation of the CME will not change obviously, as long as the total mass of the CME is approximately the same. Our simulation region contains interplanetary space, where the dynamic energy always plays

the dominant role in the process of propagation of the CME rather than the magnetic energy. Therefore, enlarging the total mass of the CME will increase its total dynamic energy and reduce the influence of background solar wind on the CME propagation in interplanetary space, which means less speed loss and greater average speed of the CME. In our work, we only simulated the propagation of a fast CME. The inner boundary of our computational region is set to 0.1 au, where the CME is launched. At this location, the CME has left the corona and basically completed its acceleration. During this stage, the influence of background solar wind on the CME is mainly deceleration rather than acceleration. If the CME is a slow one, the results should be different.

On the other hand, changing the initial magnetic field will affect the geomagnetic effect of the CME when it reaches the Earth, but will not obviously affect the dynamic process of CME propagation in interplanetary space. But the initial magnetic field will affect the expansion of the CME. In Cases 1 and 14–18 in Table 2, we can see that their arrival times are not exactly the same when the initial magnetic field changes. Moreover, we believe that during propagation in interplanetary, the dynamic process plays a dominant role, and the further the CME propagates, the more obvious this effect is. Perhaps in the early stage of propagation, due to different initial magnetic fields, the positions of the leading edge (or the arrival times) of the CMEs are different enough; however, with propagation in interplanetary space and interaction with the background solar wind, the difference caused by the initial magnetic field is gradually eliminated. One piece of evidence is that in Cases 1 and 14–18 in Table 2, the shock arrival time at the Earth is 27–29 hr, with a maximum difference of 2 hr, which is about 7%, while the shock arrival time at Mars is 57–58 hr, with a maximum difference of only 1 hr, which is about 1.7%. This result shows that the initial difference in the magnetic field intensity is gradually eliminated with increasing propagation distance.

It is well known the long duration of strong south B_z is always closely related to a major geomagnetic storm; therefore, in addition to its peak value, the duration of south B_z is also very important. Our simulation results demonstrate that not only the initial magnetic field, but also the initial mass of the CME can obviously influence the duration of south B_z. Besides, the duration of south B_z at the Earth is significantly shorter than that at Mars. Meanwhile, the peak values of both the total and z-component magnetic fields at the Earth are larger than those at Mars.

From Figure 7, we stated that, when the initial density and size of CMEs are different, similar profiles of plasma parameters can be seen by observers by keeping the total mass consistent. However, there still exist some differences in other parameters, especially in the magnetic field. For CMEs with larger initial angle δ, the magnetic field at the observers is not only higher in peak value but also longer in duration, especially at Mars.

One explanation for this difference in the peak and sustained strength of the magnetic field may be the ratio of the initial magnetic field to the initial density in the CME. When the total mass and magnetic helicity are fixed and the initial volume of the CME is varied, the density is inversely proportional to the volume of the CME, and the magnetic field is defined by Equation (6) in Section 2.2. We can estimate that when the angle δ increases, the magnetic field $B_{\max}$ does not decay as fast as the CME volume. If the total mass and magnetic helicity remain unchanged and the volume of the CME is increased, the density will decrease more than the magnetic field. We take the the CME parameters of Case 1 as the standard, and compare the density and magnetic field in Cases 10–13 through Table 3. Because of the different values of $B_{\max}$ in different parts of the CME, we choose the $B_{\max}$ value on its central axis as being representative, where the radius of the flux tube R is the maximum. From Table 3, it is obvious that with increasing δ, the volume of the CME increases, the initial density and magnetic field decrease, but the value of $B_{\max}/\rho_{\max}$ increases. Therefore, in Cases 10–13, as the CME propagates, its magnetic field with larger initial δ becomes more and more dominant than the density, so its peak value is larger than that of a CME with smaller initial δ.

Table 3
Comparison of Initial Density and Magnetic Field Strength in Case 1 and Cases 10–13

δ (deg)	Volume of CME	$\rho_{\max}$	$B_{\max}$	$B_{\max}/\rho_{\max}$
10	0.184 V_0	5.42 ρ_0	2.53 B_0	0.467 B_0/ρ_0
15	0.471 V_0	2.12 ρ_0	1.51 B_0	0.713 B_0/ρ_0
20	V_0	ρ_0	B_0	B_0/ρ_0
25	1.96 V_0	0.509 ρ_0	0.692 B_0	1.36 B_0/ρ_0
30	3.75 V_0	0.267 ρ_0	0.489 B_0	1.83 B_0/ρ_0

Note. V_0, ρ_0, and B_0 indicate the standard volume, density, and magnetic field strength of the CME in Case 1.

Besides, the difference in the velocity profiles can also be found in Figure 7, especially at Mars. We have mentioned above that the resistance of the background solar wind will slow down the propagation of a CME in interplanetary space, which is mainly due to the drag force. This drag effect on the CME can be written as (e.g., Chen 1996; Byrne et al. 2010; Maloney & Gallagher 2010)

$$M_{\rm cme}\frac{dv_{\rm cme}}{dt} = -\frac{1}{2}C_D\rho_{\rm sw}A_{\rm cme}(v_{\rm cme} - v_{\rm sw})|v_{\rm cme} - v_{\rm sw}|. \quad (17)$$

$M_{\rm cme}$ and $v_{\rm cme}$ are the total mass and velocity of the CME; $A_{\rm cme}$ is its cross-sectional area; $\rho_{\rm sw}$ and $v_{\rm sw}$ are the density and velocity of the solar wind; C_D here is called the drag coefficient. According to Equation (17), when the mass and other factors are the same, the greater the cross-sectional area of the CME, the greater the resistance it will face. In Figure 7 and Table 2, we can see that in Cases 1, 10, 11, 12, and 13, the CME with larger initial δ has a lower velocity peak at the observer, especially at Mars. As for the shock arrival times, those for CMEs with different initial δ are very close, and even CMEs with the largest initial size are slightly ahead of time by one hour. This is because, although affected by the drag force, the velocity difference between CMEs is not so distinct; moreover, the front edge of the CME with a larger initial size is also more forward and has a more significant expansion effect, which makes its arrival time the same or even shorter than those of other CMEs with smaller initial size.

In this study, we mainly focused on the influence of the initial mass (including density and thickness of the CME flux rope) and initial magnetic field (including its strength and direction) of the CME initial model based on the GCS model, and only analyzed the simulation results at observers along the

initial direction of propagation of the CME. In future research, with the continuous collection of new observational data, e.g., from Parker Solar Probe and Solar Orbiter, we may carry out more extensive case studies to test the effects of different CME initial parameters, and different solar wind backgrounds, on the simulation results at different locations in interplanetary space.

The synoptic magnetogram data in this work are obtained from the Global Oscillation Network Group (GONG) of the National Solar Observatory. The numerical calculation has been completed on TianHe-1 (A) at the National Supercomputer Center in Tianjin, China. We acknowledge the use of them. This work is jointly supported by the Strategic Priority Research Program of Chinese Academy of Sciences, Grant No. XDB 41000000, the National Natural Science Foundation of China (41774184, 41974202 and 42004146), and the Specialized Research Fund for State Key Laboratories.

ORCID iDs

Fang Shen https://orcid.org/0000-0002-4935-6679

References

Arge, C. N., Odstrcil, D., Pizzo, V. R., & Mayer, L. 2003, in AIP Conf. Proc. 679, Solar Wind Ten: Proc. Tenth Int. Solar Wind Conf. (Melville, NY: AIP), 190
Byrne, J., Maloney, S., Mcateer, J., Refojo, J., & Gallagher, P. 2010, NatCo, 1, 74
Chané, E., Jacobs, C., van der Holst, B., Poedts, S., & Kimpe, D. 2005, A&A, 432, 331
Chané, E., Poedts, S., & van der Holst, B. 2008, A&A, 492, L29
Chané, E., van der Holst, B., Jacobs, C., Poedts, S., & Kimpe, D. 2006, A&A, 447, 727
Chen, J. 1996, JGR, 101, 27499
Dasso, S., Mandrini, C., Demoulin, P., & Luoni, M. 2006, A&A, 455, 349
Feng, X., Yang, L., Xiang, C., et al. 2010, ApJ, 723, 300
Gibson, S. C., & Low, B. 1998, ApJ, 493, 460
Gonzalez, W., Echer, E., Gonzalez, A., & Tsurutani, B. 2011, AGU Fall Meeting, SM54B-02
Gonzalez, W., Joselyn, J., Kamide, Y., et al. 1994, JGR, 99, 5771
Gosling, J. J., Bame, S., McComas, D. L., & Phillips, J. 1990, GeoRL, 17, 901
Hosteaux, S., Chané, E., & Poedts, S. 2019, A&A, 632, A89
Howard, R. J., Michels, D. S. J., & Koomen, M. 1982, ApJ, 263, L101
Liu, Y., Shen, F., & Yang, Y. 2019, ApJ, 887, 150
Liu, Y., Thernisien, A., Luhmann, J., et al. 2010, ApJ, 722, 1762
Lundquist, S. 1951, PhRv, 83, 307
Lynch, B., Li, Y., Thernisien, A., et al. 2010, JGRA, 115, 7106
Maloney, S., & Gallagher, P. 2010, ApJL, 724, L127
Manchester, W. B., Gombosi, T., Roussev, I., et al. 2004a, JGR, 109, A01104
Manchester, W. B., Gombosi, T., Roussev, I., et al. 2004b, JGR, 109, A02107
Odstrcil, D., & Pizzo, V. 1999, JGR, 104, 28225
Patsourakos, S., Vourlidas, A., & Kliem, B. 2010, A&A, 522, A100
Pomoell, J., & Poedts, S. 2018, JSWSC, 8, A35
Poomvises, W., Zhang, J., & Olmedo, a. 2010, ApJL, 717, L159
Scolini, C., Verbeke, C., Poedts, S., et al. 2018, SpWea, 16, 754
Shen, C., Wang, Y., Pan, Z., et al. 2014a, JGRA, 119, 5107
Shen, F., Feng, X., Wu, S., Xiang, C. B., & Song, W. 2011, JGRA, 116, A09103
Shen, F., Shen, C., Zhang, J., et al. 2014b, JGRA, 119, 7128
Shen, F., Yang, Z., Zhang, J., Wei, W., & Feng, X. 2018, ApJ, 866, 18
Thernisien, A. 2011, ApJS, 194, 33
Thernisien, A., Howard, R., & Vourlidas, A. 2006, ApJ, 652, 763
Thernisien, A., Vourlidas, A., & Howard, R. 2009, SoPh, 256, 111
Xue, X., Wang, C., & Dou, X. 2005, JGRA, 110, A08103
Zhang, J., Richardson, I., Webb, D., et al. 2007, JGRA, 112, 10102
Zhao, X., Hansen, W., Plunkett, S., & Liu, W. 2002, JGRA, 107, 1223
Zhou, Y., & Feng, X. 2016, JGRA, 122, 1451